

# LucidNFT: LR-Anchored Multi-Reward Preference Optimization for Generative Real-World Super-Resolution

Song Fei<sup>1</sup><sup>†</sup>, Tian Ye<sup>1</sup><sup>†</sup>, Sixiang Chen<sup>1</sup>, Zhaohu Xing<sup>1</sup>, Jianyu Lai<sup>1</sup>, and Lei Zhu<sup>1,2</sup><sup>\*</sup>

<sup>1</sup> The Hong Kong University of Science and Technology (Guangzhou), Guangzhou, China

<sup>2</sup> The Hong Kong University of Science and Technology, Hong Kong SAR, China  
{sfei285, tye610, schen691, zxing565, jlai218}@connect.hkust-gz.edu.cn  
leizhu@hkust-gz.edu.cn

**Abstract.** Generative real-world image super-resolution (Real-ISR) can synthesize visually convincing details from severely degraded low-resolution (LR) inputs, yet its stochastic sampling makes a critical failure mode hard to avoid: outputs may look sharp but be *unfaithful* to the LR evidence (semantic and structural hallucination), while such LR-anchored faithfulness is difficult to assess without HR ground truth. Preference-based reinforcement learning (RL) is a natural fit because each LR input yields a *rollout group* of candidates to compare. However, effective alignment in Real-ISR is hindered by (i) the lack of a degradation-robust *LR-referenced* faithfulness signal, and (ii) a rollout-group optimization bottleneck where naive multi-reward scalarization followed by normalization compresses objective-wise contrasts, causing *advantage collapse* and weakening the reward-weighted updates in DiffusionNFT-style forward fine-tuning. Moreover, (iii) limited coverage of real degradations restricts rollout diversity and preference signal quality. We propose **LucidNFT**, a multi-reward RL framework for *flow-matching* Real-ISR. LucidNFT introduces **LucidConsistency**, a degradation-robust semantic evaluator that makes LR-anchored faithfulness measurable and optimizable; a **de-coupled advantage normalization** strategy that preserves objective-wise contrasts *within each LR-conditioned rollout group* before fusion, preventing advantage collapse; and **LucidLR**, a large-scale collection of real-world degraded images to support robust RL fine-tuning. Experiments show that LucidNFT consistently improves strong flow-based Real-ISR baselines, achieving better perceptual-faithfulness trade-offs with stable optimization dynamics across diverse real-world scenarios.

**Keywords:** Real-World Super-Resolution · Preference Optimization

---

<sup>†</sup> Equal contribution    <sup>\*</sup> Corresponding author

## 1 Introduction

Real-world image super-resolution (Real-ISR) aims to recover a high-resolution (HR) image from a degraded low-resolution (LR) observation under *unknown* and *heterogeneous* degradations. Empowered by large-scale generative priors, recent generative Real-ISR approaches—including diffusion-based methods [2, 19, 33, 35, 39, 43, 44] and scalable flow-matching formulations [10, 13]—have substantially improved perceptual restoration quality by synthesizing rich and plausible high-frequency details beyond regression-based frameworks [7, 9, 47]. However, this generative freedom also exposes a central reliability bottleneck: restored details may look realistic yet be *unfaithful* to the LR evidence (i.e., semantic or structural hallucination [8]). In the absence of HR ground truth, we often lack a reliable way to *measure* and therefore *optimize* such LR-anchored faithfulness, which becomes a key obstacle for deploying and aligning generative Real-ISR models in the wild.

Interestingly, stochastic sampling is not only the source of hallucination but also a source of supervision. For a fixed LR input, a generative Real-ISR model can produce multiple candidate restorations by varying noise seeds, naturally forming a preference set that spans different perceptual–faithfulness trade-offs. This structure suggests preference-driven reinforcement learning (RL) [29]: we could promote candidates that are both perceptually strong and faithful to the LR observation, while suppressing those that hallucinate inconsistent structures.

Yet, making preference optimization effective for Real-ISR is fundamentally non-trivial. Beyond the need for a faithfulness signal, Real-ISR introduces a *rollout-group* learning structure that standard multi-reward RL pipelines do not handle well. Specifically, preference learning compares multiple rollouts *conditioned on the same LR input*, where candidates can excel in different objectives. In this setting, a common practice—scalarizing multiple rewards into a single score followed by normalization [21, 41, 48]—can destroy the very contrasts that distinguish meaningful perceptual–faithfulness trade-offs. Perceptual metrics and faithfulness measures often have different scales and variance patterns; when they are fused *before* normalization, dominant components can overshadow others, and rollouts with distinct trade-offs may collapse to similar normalized advantages. This *advantage collapse* is particularly harmful under DiffusionNFT-style forward fine-tuning, where the bounded reward weight directly modulates the relative strength of positive and negative velocity perturbations: once the advantage contrast is compressed, the reward weight loses effective dynamic range, weakening preference guidance and making it easy for faithfulness to be drowned out by perceptual objectives.

In addition to this optimization bottleneck, two practical conditions are required to make RL alignment meaningful for Real-ISR. First, without HR references, common no-reference perceptual metrics [15, 30, 32, 38, 42, 46] are not designed to evaluate LR-anchored faithfulness; optimizing them alone can inadvertently reward over-sharpening and hallucinated textures. Real-ISR thus needs an *LR-referenced* faithfulness signal that is robust to unknown degradations. Second, RL relies on informative rollouts to provide meaningful preference

comparisons. Existing Real-ISR datasets are often paired but limited in scale and capture conditions [4, 37], while synthetic degradation pipelines [1, 34] may not reflect the diversity and entanglement of degradations in real-world data, restricting rollout diversity and the strength of preference signals.

To address these challenges, we propose **LucidNFT**, a multi-reward RL framework for aligning flow-matching Real-ISR models. LucidNFT is built around three tightly coupled components that make preference learning *faithfulness-first* and *rollout-group effective*:

- **LucidConsistency**, a degradation-robust semantic evaluator that provides an *LR-anchored faithfulness* score between LR inputs and SR outputs, enabling preference optimization without HR supervision.
- **Decoupled multi-reward advantage normalization**, which preserves objective-wise reward contrasts *within each LR-conditioned rollout group* before fusion, preventing advantage collapse and ensuring that faithfulness is not drowned out by perceptual objectives during RL optimization.
- **LucidLR**, a large-scale collection of real-world degraded images that supplies diverse degradations to produce informative rollouts and stable preference learning. We will publicly release the dataset.

Extensive experiments demonstrate that LucidNFT consistently improves strong flow-based Real-ISR baselines, yielding better perceptual–faithfulness trade-offs with stable optimization dynamics under diverse real degradations.

## 2 Related Work

### 2.1 Generative Real-World Image Super-Resolution

Early Real-ISR methods mainly rely on regression-based models [7, 9, 47] or GAN-based frameworks [34, 45], which learn deterministic mappings from LR to HR images. While effective for synthetic degradations, these approaches often struggle to synthesize realistic textures under complex real-world degradation patterns. Recent advances increasingly adopt large-scale generative models for Real-ISR. Diffusion-based methods [2, 19, 33, 35, 39, 43, 44] leverage pretrained text-to-image priors [6, 11, 16, 25, 27] to synthesize perceptually rich details beyond regression-based approaches. More recently, flow-based generative formulations [10, 13] improve scalability and sampling efficiency by learning velocity fields under the flow-matching framework. Although these generative models enable diverse candidate reconstructions through stochastic sampling, the generated details may deviate from the structural content of the LR input, resulting in hallucinated structures. Maintaining semantic faithfulness to the LR observation remains an open challenge in generative Real-ISR.

### 2.2 Evaluation Methods for Real-World Image Super-Resolution

Evaluating Real-ISR outputs is challenging since ground-truth HR images are rarely available in real-world scenarios. Full-reference metrics such as PSNR and

SSIM [36] require paired HR supervision and are therefore unsuitable for realistic settings. Consequently, no-reference image quality assessment (NR-IQA) methods [15, 30, 42, 46] are widely adopted to evaluate perceptual quality without HR references. Recent works further introduce CLIP-based [32] and vision–language-model variant evaluators [32, 38] to incorporate semantic-aware quality assessment. These metrics primarily assess perceptual realism but provide limited capability to measure whether restored details remain consistent with the LR input. As a result, visually plausible yet semantically inconsistent reconstructions may still obtain high perceptual scores.

### 2.3 Reinforcement Learning for Vision Generation Models

Reinforcement learning has recently been explored to align generative models with external objectives. Denoising Diffusion Policy Optimization (DDPO) [3] formulates diffusion sampling as a sequential decision process and optimizes the denoising policy using PPO-style [28] updates. Preference-based alignment approaches such as Diffusion-DPO [31] extend Direct Preference Optimization (DPO) [26] to diffusion models, enabling optimization from pairwise preference comparisons without explicit policy-gradient estimation. Diffusion Negative-aware Finetuning (DiffusionNFT) [48] introduces a forward-consistent reinforcement learning framework compatible with velocity parameterization and flow-based generative models. Instead of applying policy gradients along reverse diffusion trajectories, DiffusionNFT integrates reward signals directly into the forward flow-matching objective through implicit velocity perturbations, enabling stable fine-tuning. Despite these advances, applying RL-based alignment to Real-ISR introduces additional challenges. Restoration quality is inherently multi-objective, involving perceptual realism and LR-conditioned structural faithfulness. Existing approaches [21, 41, 48] typically aggregate heterogeneous rewards into a single scalar signal prior to normalization, which may obscure objective-specific differences and weaken preference discrimination.

### 2.4 Real-World Image Super-Resolution Datasets

Training and evaluating Real-ISR models requires datasets that reflect realistic degradation patterns. Synthetic pipelines such as Real-ESRGAN [34] simulate degradations including blur, noise, and compression artifacts on high-quality datasets such as DIV2K, Flickr2K [1], and LSDIR [18]. While effective for supervised training, synthetic degradations often fail to capture the complexity of real-world imaging artifacts. Several datasets provide real LR–HR image pairs captured under specialized acquisition setups, including RealSR [4] and DRealSR [37]. Although valuable for benchmarking, their scale and degradation diversity remain limited. Such limitations restrict their suitability for large-scale reinforcement learning, where diverse degraded inputs are necessary to generate meaningful rollout variations and preference signals.

### 3 Preliminaries

#### 3.1 Flow Matching

Flow matching [20, 22] learns a continuous transport map between a source distribution and a target data distribution through a velocity field. Given a data sample  $x_0 \sim \mathcal{X}_0$  and a Gaussian sample  $x_1 \sim \mathcal{X}_1$ , rectified flow constructs a linear interpolation  $x_t = (1 - t)x_0 + tx_1$ ,  $t \in [0, 1]$ . The corresponding velocity field is defined as  $v = x_1 - x_0$ . A neural network  $v_\theta(x_t, t, c)$  is trained to approximate this velocity by minimizing the flow-matching objective

$$\mathcal{L}_{\text{FM}}(\theta) = \mathbb{E}_{t, x_0, x_1} [\|v - v_\theta(x_t, t, c)\|_2^2]. \quad (1)$$

For conditional generation tasks such as Real-ISR, the velocity field is conditioned on an observed input  $c$ , enabling the model to learn a transport map from noise to structured outputs guided by the LR observation.

#### 3.2 Diffusion Negative-aware FineTuning

DiffusionNFT [48] performs direct policy optimization on the forward diffusion process by leveraging a reward signal  $r(x_0, c) \in [0, 1]$ . Unlike standard policy-gradient formulations [21, 41] that optimize reverse-time likelihoods, DiffusionNFT introduces a contrastive diffusion objective that explicitly encourages the velocity predictor to move toward high-reward behaviors and away from low-reward behaviors within the forward flow matching framework. Given a frozen offline policy  $v_{\text{old}}$ , DiffusionNFT constructs implicit positive and negative policies:

$$v_\theta^+(x_t, t, c) = (1 - \beta)v_{\text{old}}(x_t, t, c) + \beta v_\theta(x_t, t, c), \quad (2)$$

$$v_\theta^-(x_t, t, c) = (1 + \beta)v_{\text{old}}(x_t, t, c) - \beta v_\theta(x_t, t, c), \quad (3)$$

where  $\beta$  controls the guidance strength. These perturbations can be interpreted as shifting the reference velocity field along the improvement direction  $v_\theta - v_{\text{old}}$ . The training objective is defined as

$$\mathcal{L}(\theta) = \mathbb{E}_{c, x_0 \sim \pi_{\text{old}}, t} [\|v_\theta^+ - v\|_2^2 + (1 - r)\|v_\theta^- - v\|_2^2], \quad (4)$$

where  $v$  denotes the ground-truth velocity target. High-reward samples emphasize the positive perturbation term, while low-reward samples increase the contribution of the negative term, forming a reward-weighted contrastive update in velocity space. To stabilize optimization, rewards are normalized as

$$r(x_0, c) = \frac{1}{2} + \frac{1}{2} \text{clip} \left( \frac{r_{\text{raw}}(x_0, c) - \mathbb{E}_{\pi_{\text{old}}}[r_{\text{raw}}]}{Z_c}, -1, 1 \right), \quad (5)$$

where  $Z_c$  controls the global reward scale. By embedding reward-weighted contrast directly into the forward velocity objective, DiffusionNFT preserves forward-process consistency, avoids explicit likelihood approximation, and enables stable fine-tuning of high-dimensional diffusion and flow-based generative models.

## 4 Method

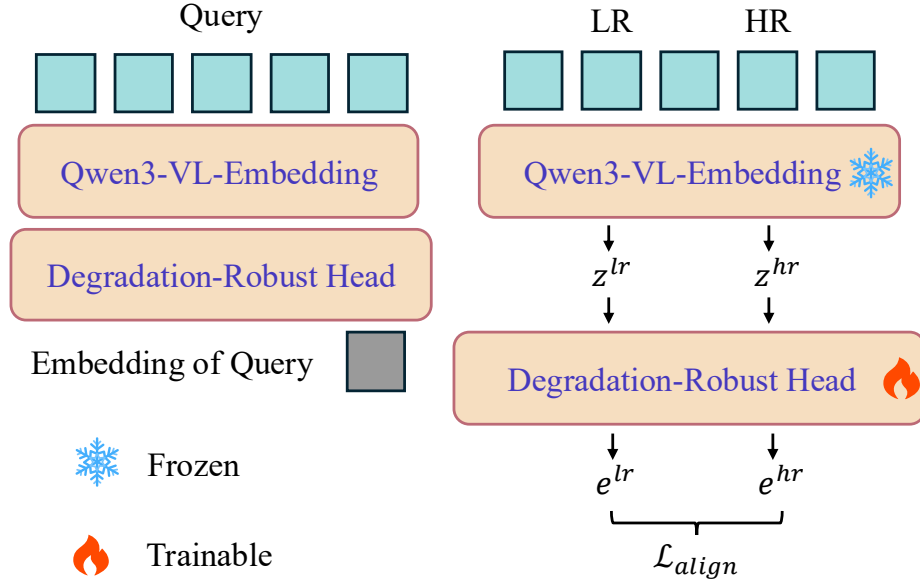


**Fig. 1:** Overview of **LucidConsistency**. Left: inference stage where embeddings of the LR input and SR output are extracted and their semantic consistency is computed via Eq. (10). Right: training stage where LR–HR pairs are used to optimize the projection head.

### 4.1 LucidConsistency: Degradation-Robust Consistency Evaluation

Existing Real-ISR evaluation protocols mainly rely on no-reference perceptual metrics [15, 30, 32, 38, 42, 46], which cannot assess whether restored content remains faithful to the LR observation when HR references are unavailable. We therefore seek an *LR-referenced* faithfulness signal by comparing LR and SR in a shared semantic space. A key challenge is degradation-induced embedding shift: LR inputs with unknown and complex degradations may occupy different regions from clean images even when semantics are preserved, making direct similarity unreliable.

To address this, we propose **LucidConsistency**, a degradation-*robust* semantic evaluator that aligns representations across degradation levels. We build on a pretrained multimodal embedding backbone  $E(\cdot)$  (Qwen3-VL-Embedding [17]), which is frozen to preserve its pretrained semantic structure. We then learn a lightweight projection head  $g(\cdot)$  to map embeddings into a degradation-aligned space. All images are resized to the backbone’s required input resolution before

encoding, so the resulting score reflects representation-level semantic alignment rather than pixel-level sharpness.

Given paired training samples  $(x_i^{lr}, x_i^{hr})$ , we compute

$$z_i^{lr} = E(x_i^{lr}), \quad z_i^{hr} = E(x_i^{hr}), \quad (6)$$

and project them as

$$e_i^{lr} = g(z_i^{lr}), \quad e_i^{hr} = g(z_i^{hr}). \quad (7)$$

We optimize  $g(\cdot)$  with symmetric InfoNCE [24] to align matched LR/HR pairs while maintaining inter-instance separability:

$$\mathcal{L}_{align} = \frac{1}{2} (\mathcal{L}_{lr \rightarrow hr} + \mathcal{L}_{hr \rightarrow lr}), \quad (8)$$

where

$$\mathcal{L}_{lr \rightarrow hr} = -\frac{1}{B} \sum_{i=1}^B \log \frac{\exp(s(e_i^{lr}, e_i^{hr})/\tau)}{\sum_{j=1}^B \exp(s(e_i^{lr}, e_j^{hr})/\tau)}. \quad (9)$$

$\mathcal{L}_{hr \rightarrow lr}$  is defined symmetrically by swapping queries and targets. After training, LucidConsistency defines the LR-anchored faithfulness score between an LR input  $x_{lr}$  and a generated SR output  $x_{sr}$  as

$$\mathcal{C}(x_{lr}, x_{sr}) = s(g(E(x_{lr})), g(E(x_{sr}))), \quad (10)$$

where  $s(\cdot, \cdot)$  denotes cosine similarity. This score serves as both an evaluation metric and a reward component for RL fine-tuning.

While the learned alignment substantially reduces degradation-induced embedding shift, any LR-referenced similarity can still be confounded under *under-restoration*, where the SR output preserves LR-like degradation appearance. We analyze this degradation-overlap effect and its mitigation in Sec. 5.3.

## 4.2 Multi-Reward Reinforcement Learning for Real-ISR

Stochastic sampling yields multiple rollouts per LR input, spanning different perceptual-faithfulness trade-offs. Under DiffusionNFT, the learning signal is a bounded reward weight  $r \in [0, 1]$  that modulates the contrastive forward objective. The key challenge is to combine multiple objectives into a discriminative *rollout-group* preference signal without collapsing objective-wise contrasts.

**Notation.** Let  $x_i$  denote the  $i$ -th LR input ( $i = 1, \dots, N$ ), and  $y_{i,j}$  its  $j$ -th rollout ( $j = 1, \dots, M_i$ ). For each rollout we compute a  $K$ -dimensional reward vector

$$\mathbf{r}_{i,j} = \left( r_{i,j}^{(1)}, \dots, r_{i,j}^{(K)} \right) \in \mathbb{R}^K, \quad (11)$$

with fixed objective weights  $\lambda_k$ .

**Scalar-first aggregation (baseline).** A standard approach first scalarizes rewards:

$$s_{i,j} = \sum_{k=1}^K \lambda_k r_{i,j}^{(k)}. \quad (12)$$

It then applies rollout-group centering with batch-global scaling:

$$A_{i,j} = \frac{s_{i,j} - \mu_i}{\sigma_{\text{global}} + \epsilon}, \quad \mu_i = \frac{1}{M_i} \sum_{j=1}^{M_i} s_{i,j}, \quad (13)$$

$$\sigma_{\text{global}} = \text{Std}(\{s_{p,q}\}_{(p,q) \in \mathcal{B}}), \quad (14)$$

followed by a bounded mapping to the reward weight  $r \in [0, 1]$ . In Real-ISR, objectives often differ in scale and variance (e.g., smooth IQA vs. sensitive structural faithfulness). When fused *before* normalization, dominant objectives can suppress others, making rollouts with different trade-offs receive similar normalized scores—*advantage collapse*—and weakening preference learning.

**LucidNFT: decoupled normalization before fusion.** To preserve objective-wise contrasts *within each LR-conditioned rollout group*, we normalize each objective per group before fusion. For each objective  $k$ :

$$\mu_i^{(k)} = \frac{1}{M_i} \sum_{j=1}^{M_i} r_{i,j}^{(k)}, \quad \sigma_i^{(k)} = \text{Std}(\{r_{i,j}^{(k)}\}_{j=1}^{M_i}), \quad (15)$$

$$z_{i,j}^{(k)} = \frac{r_{i,j}^{(k)} - \mu_i^{(k)}}{\sigma_i^{(k)} + \epsilon}. \quad (16)$$

We then fuse normalized objectives:

$$\tilde{a}_{i,j} = \sum_{k=1}^K \lambda_k z_{i,j}^{(k)}, \quad (17)$$

and stabilize the signal with batch-level normalization:

$$A_{i,j}^L = \frac{\tilde{a}_{i,j} - \mu_{\text{batch}}}{\sigma_{\text{batch}} + \epsilon}, \quad (18)$$

where  $\mu_{\text{batch}}$  and  $\sigma_{\text{batch}}$  are computed over  $\{\tilde{a}_{p,q}\}_{(p,q) \in \mathcal{B}}$ .

**Mapping to the DiffusionNFT reward weight.** Following DiffusionNFT’s reward mapping form (Eq. (5)), we convert  $A_{i,j}^L$  into the bounded reward weight  $r_{i,j}^L \in [0, 1]$  and *only* replace the input with  $A_{i,j}^L$ :

$$r_{i,j}^L = \frac{1}{2} + \frac{1}{2} \text{clip}\left(\frac{A_{i,j}^L}{Z_c}, -1, 1\right). \quad (19)$$

We directly substitute  $r_{i,j}^L$  for the reward weight  $r_{i,j}$  in the DiffusionNFT objective (Eq. (4)), keeping all other terms unchanged. No additional min–max rescaling or post-hoc normalization is applied beyond Eq. (19). This normalize-then-aggregate design preserves objective-specific variation before fusion, improving sensitivity to perceptual–faithfulness trade-offs and reducing advantage collapse.

To quantify advantage separability, we randomly sample 100 images from RealLQ250 [2] and generate  $M$  stochastic rollouts per image ( $M \in [2, 16]$ ). For each rollout group, we identify the pair with the largest reward discrepancy  $\Delta r$  and measure the corresponding advantage gap  $|\Delta A|$ . We also report the Distinct Advantage Group Count (DAGC), defined as the number of distinct advantage levels within each rollout group. As shown in Fig. 2, LucidNFT consistently yields larger  $|\Delta A|$  and higher DAGC than DiffusionNFT, indicating improved advantage separability.

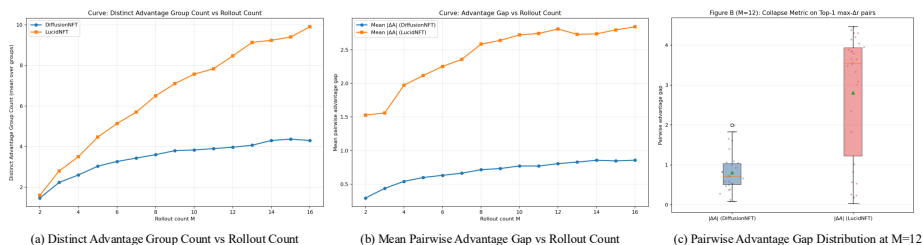


**Fig. 2:** Advantage separability analysis on the LucidFlux backbone using dataset RealLQ250 [2]. (a) DAGC versus rollout count  $M$ ; (b) mean pairwise advantage gap  $|\Delta A|$  versus  $M$  using the top-1 max- $\Delta r$  pair per group; (c) distribution of  $|\Delta A|$  at  $M = 12$ . LucidNFT consistently yields larger advantage gaps and higher separability than DiffusionNFT, indicating reduced advantage compression under decoupled normalization.

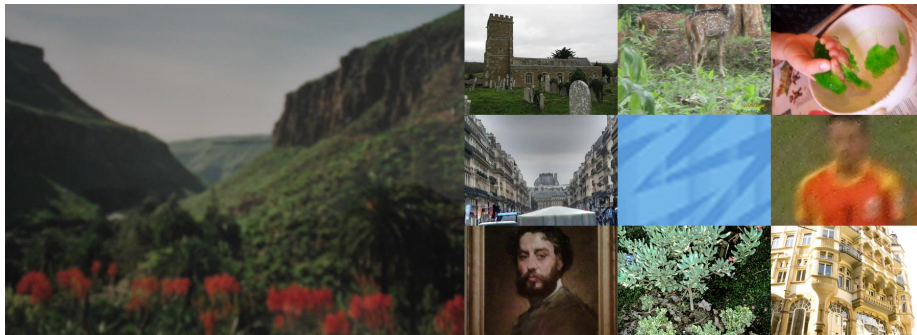


**Fig. 3:** Representative examples from **LucidLR**.

### 4.3 LucidLR: A Large-Scale Real-World Degradation Dataset for Real-ISR

Table 1 summarizes representative Real-ISR datasets and highlights the scale and usage gap that motivates LucidLR for RL fine-tuning. RL-based alignment

**Table 1:** Comparison of representative real-world datasets used in Real-ISR. Existing datasets are mainly designed for benchmarking and contain limited samples, while LucidLR provides large-scale real-world degradations suitable for RL-based training.

Dataset	Pairing	Primary Usage	Type	# Images
RealSR [4]	Paired	Testing / Benchmark	Real-captured	100
DRealSR [37]	Paired	Testing / Benchmark	Real-captured	93
RealLQ250 [2]	Unpaired	Testing / Benchmark	Real-world	250
<b>LucidLR (ours)</b>	Unpaired	RL/Unsupervised Training	Real-world	20K

benefits from diverse real-world degradations that induce informative rollout variations and reward contrasts. Existing Real-ISR datasets [4,37] are primarily designed for benchmarking and contain paired images captured under controlled protocols, limiting their scale and degradation diversity for RL fine-tuning. We therefore construct **LucidLR**, a large-scale real-world low-quality dataset collected from Wikimedia Commons via its official API. Images are gathered from public categories such as *Images of low quality* and *Blurred images*, which contain naturally occurring degradations (motion/defocus blur, compression artifacts, etc.). According to the Wikimedia Commons licensing policy, these images are publicly available and can be freely used with proper attribution. The raw pool contains  $\sim 22\text{K}$  images and may include a small portion of inappropriate content; we apply a pretrained NSFW classifier [12] and remove images with predicted probability  $P_{\text{NSFW}} \geq 0.2$ , along with corrupted files, and manually review the remaining images to remove inappropriate samples. After filtering, LucidLR contains 20K real-world degraded images (Fig. 3). Detailed statistics of degradation categories and their proportion distribution, along with the IQA score distribution of the dataset, are provided in the supplementary material.

## 5 Experiment

### 5.1 Implementation Details

For **LucidConsistency**, we adopt Qwen3-VL-Embedding-8B [17] as the backbone with a lightweight projection head consisting of two linear layers and a GELU activation. The model is trained on synthesized LR–HR pairs generated from LSDIR [18] using the Real-ESRGAN [34] degradation pipeline. Training is performed on 2 NVIDIA A100 GPUs for 4,000 steps with a learning rate of  $1 \times 10^{-4}$ , batch size 8, temperature  $\tau = 0.7$  in Eq. 9, and input resolution 512. For **LucidNFT**, we fine-tune the base model using LoRA [14] (rank 32) on the LucidLR dataset. Training runs on 8 NVIDIA A100 GPUs for 600 steps with a learning rate of  $3 \times 10^{-5}$  and batch size 3, sampling 12 rollouts per LR input. The sampling resolution is set to 768 with 6 inference steps. We adopt EMA with decay 0.9 and a KL regularization weight of  $1 \times 10^{-4}$ . We use UniPercept IQA [5] as the perceptual reward and LucidConsistency as the semantic reward, both with

**Table 2:** Cosine similarity between LR–HR image pairs under correct pairing and cross-bench swapped pairing. LucidConsistency improves alignment on correctly paired data while maintaining low similarity under mismatched pairing.

Domain	Dataset Pairing	Baseline	LucidConsistency
Synthetic	LSDIR-Val (paired)	0.759	0.890 (+0.131)
Real-World	RealSR	0.799	0.925 (+0.126)
	DRealSR	0.786	0.921 (+0.135)
Cross-Bench	RealSR LR $\leftrightarrow$ DRealSR HR	0.144	0.100 (-0.044)
	DRealSR LR $\leftrightarrow$ RealSR HR	0.140	0.131 (-0.009)

weight 1, which empirically provides a balanced trade-off between perceptual quality and LR-faithfulness. Both methods are optimized using AdamW [23].

## 5.2 Effectiveness of Degradation-Robust Semantic Alignment for LucidConsistency

We evaluate the proposed degradation-robust semantic alignment by measuring cosine similarity between paired LR–HR images. For correctly paired datasets, LR and HR images depict the same scene content under different degradation levels; thus a desirable evaluator should assign consistently higher similarity to matched pairs than to mismatched pairs, while remaining sensitive to content mismatches. We conduct experiments on one synthetic domain (LSDIR-Val [18], generated using the Real-ESRGAN [34] degradation pipeline) and two real-world datasets (RealSR [4] and DRealSR [37]). We compare the frozen Qwen3-VL-Embedding backbone with our projection head (LucidConsistency). As shown in Table 2, LucidConsistency consistently increases cosine similarity on correctly paired datasets across both synthetic and real-world domains. We further conduct a cross-bench swap experiment by pairing LR images from one dataset with HR images from another. Similarity scores remain low under mismatched pairing for both the backbone and LucidConsistency, indicating that the learned projection does not collapse semantic discrimination. Taken together, these results suggest that the learned projection reduces degradation-induced embedding shift while preserving content sensitivity in the representation space.

## 5.3 Effectiveness of LucidNFT

We evaluate LucidNFT on two representative flow-based Real-ISR models, LucidFlux [13] and DiT4SR [10]. LucidFlux is built upon a large-scale DiT-based generative backbone (14B total parameters, including a 12B flow prior), whereas DiT4SR adopts a comparatively lightweight DiT-based architecture derived from stable-diffusion-3-medium [11], with a 2B prior and a 2.72B adapter. Fig. 4 shows the training dynamics of LucidNFT on LucidFlux. Both the image quality reward (UniPercept IQA) and the consistency reward (LucidConsistency) exhibit stable

optimization behavior throughout training. Despite the stochasticity introduced by generative sampling, the smoothed reward curves demonstrate a clear upward trend, indicating that LucidNFT effectively improves perceptual quality while preserving structural consistency. The evaluation rewards on the validation set follow a similar pattern. Both metrics steadily increase and gradually converge as training progresses, suggesting that the learned policy generalizes beyond the training samples and avoids reward overfitting. Due to space constraints, additional experiments on DiT4SR are provided in the supplementary material. We observe similar optimization dynamics when applying LucidNFT to DiT4SR, with the corresponding training curves included for reference. These results further demonstrate the effectiveness of LucidNFT across flow-based generative backbones of different scales.



**Fig. 4:** Training dynamics of LucidNFT on LucidFlux. From left to right: training LucidConsistency score, evaluation LucidConsistency score, training UniPercept IQA score, and evaluation UniPercept IQA score. The smoothed curves exhibit a consistent upward trend, indicating stable multi-reward optimization during RL.

**Comparison Methods and Evaluation Metrics.** We compare the LucidNFT-optimized model (LucidFlux + LucidNFT) with several representative generative SR methods, including ResShift [44], StableSR [33], SinSR [35], DiffBIRv2 [19], SeeSR [39], DreamClear [2], SUPIR [43], DiT4SR [10], as well as the baseline LucidFlux [13]. All methods are evaluated at an output resolution of  $1024 \times 1024$  with a  $4\times$  upscaling factor. For each baseline, we follow the official implementations and recommended inference settings provided by the authors to ensure fair comparison. We evaluate all methods using nine NR-IQA metrics, including CLIP-IQA+ [32], Q-Align [38], MUSIQ [15], MANIQA [42], NIMA [30], CLIP-IQA [32], NIQE [46], UniPercept IQA [5], and VisualQuality-R1 (VQ-R1) [40]. To further measure the faithfulness between the restored image and the input LR observation, we also report our proposed **LucidConsistency**, which evaluates input-output structural consistency without requiring HR ground truth.

**Quantitative Comparison.** Table 3 reports quantitative results on RealLQ250 [2], DRealSR [37], and RealSR [4]. Built upon the strong LucidFlux baseline, LucidFlux(+LucidNFT) consistently improves most perceptual quality metrics across all datasets. For example, on RealLQ250, our method improves MUSIQ from 72.33 to 73.45 and UniPercept from 70.93 to 73.48, while reducing NIQE from 3.74 to 3.25. Similar improvements are observed on DRealSR and RealSR, where

**Table 3:** Quantitative comparison with state-of-the-art Real-ISR methods on RealLQ250 [2], DRealSR [37], and RealSR [4]. Higher is better for all metrics except NIQE. Values in the last column show improvements relative to the LucidFlux baseline.

Benchmark	Metric	ResShift	StableSR	SinSR	DiffBIRv2	SeeSR	DreamClear	SUPIR	DIT4SR	LucidFlux	LucidFlux(+LucidNFT)
RealLQ250	CLIP-IQA+ $\uparrow$	0.5529	0.5804	0.6054	0.6919	0.7034	0.6813	0.6532	0.7098	0.7208	<b>0.7465</b> (+0.0257)
	Q-Align $\uparrow$	3.6318	3.5583	3.7451	3.9755	4.1423	4.0647	4.1347	4.2270	4.4052	<b>4.4855</b> (+0.0803)
	MUSIQ $\uparrow$	59.5032	57.2517	65.4543	67.5313	70.3757	67.0899	65.8133	71.6682	72.3351	<b>73.4475</b> (+1.1124)
	MANIQA $\uparrow$	0.3397	0.2937	0.4230	0.4900	0.4895	0.4405	0.3826	0.4607	0.5227	<b>0.5443</b> (+0.0216)
	NIMA $\uparrow$	5.0624	5.0538	5.2397	5.3132	5.3146	5.2209	5.0806	5.4765	<b>5.6050</b>	5.5669 (+0.0381)
	CLIP-IQA $\uparrow$	0.6129	0.5160	0.7166	0.7137	0.7063	0.6957	0.5767	0.7141	0.6855	<b>0.7233</b> (+0.0378)
	NIQE $\downarrow$	6.6326	4.6236	5.4425	5.1193	4.4383	3.8709	3.6591	3.5556	3.7410	<b>3.2532</b> (-0.4878)
	UniPercept IQA $\uparrow$	58.9290	57.6015	62.7525	65.4760	69.2015	68.8465	68.6430	73.0740	70.9300	<b>73.4790</b> (+2.5490)
	VisualQuality-R1 $\uparrow$	4.0911	3.9474	3.9044	4.3428	4.5118	4.4430	4.4265	4.6146	4.5474	<b>4.6510</b> (+0.1036)
LucidConsistency $\uparrow$	0.9340	<b>0.9496</b>	0.9232	0.9430	0.9352	0.9467	0.9376	0.9359	0.9334	<b>0.9366</b> (+0.0032)	
DRealSR	CLIP-IQA+ $\uparrow$	0.4655	0.3732	0.5402	0.6476	0.6258	0.4462	0.5494	0.6537	0.6516	<b>0.6867</b> (+0.0351)
	Q-Align $\uparrow$	2.6312	2.1243	3.1336	3.0487	3.2746	2.4214	3.4722	3.6008	3.7141	<b>3.8423</b> (+0.1282)
	MUSIQ $\uparrow$	40.9795	29.6691	53.9139	60.0759	61.3222	35.1912	54.9280	63.8051	64.6025	<b>68.1545</b> (+3.5520)
	MANIQA $\uparrow$	0.2688	0.2402	0.3456	0.4900	0.4505	0.2676	0.3483	0.4419	0.4678	<b>0.5004</b> (+0.0326)
	NIMA $\uparrow$	4.3179	3.9049	4.6227	4.6543	4.6402	3.9369	4.5064	4.9913	4.9560	<b>4.9968</b> (+0.0408)
	CLIP-IQA $\uparrow$	0.4964	0.3383	0.6632	0.6782	0.6760	0.4361	0.5310	0.6732	0.6673	<b>0.7073</b> (+0.0400)
	NIQE $\downarrow$	10.3006	8.6023	6.9800	6.4853	6.4503	7.0164	5.9092	5.7001	5.0742	<b>4.1788</b> (-0.8954)
	UniPercept IQA $\uparrow$	37.3199	26.0659	49.2755	46.2298	50.3414	34.2473	55.1371	58.1290	59.9032	<b>63.7782</b> (+3.8750)
	VisualQuality-R1 $\uparrow$	3.0231	1.8758	3.3868	3.4796	3.6116	2.5655	3.7349	3.9603	3.9955	<b>4.1455</b> (+0.1500)
LucidConsistency $\uparrow$	0.8897	<b>0.9413</b>	0.8604	0.7725	0.8926	0.9403	0.8909	0.8886	0.7998	<b>0.7916</b> (-0.0082)	
RealSR	CLIP-IQA+ $\uparrow$	0.5005	0.4408	0.5416	0.6543	0.6731	0.5331	0.5640	0.6753	0.6669	<b>0.7151</b> (+0.0482)
	Q-Align $\uparrow$	3.1041	2.5086	3.3614	3.3156	3.6073	3.0040	3.4682	3.7106	3.8728	<b>3.9918</b> (+0.1190)
	MUSIQ $\uparrow$	49.4988	39.9816	57.9502	61.7751	67.5660	49.4766	55.6807	67.9828	67.8962	<b>70.5625</b> (+2.6663)
	MANIQA $\uparrow$	0.2976	0.2356	0.3753	0.4745	0.5087	0.3092	0.3426	0.4533	0.4889	<b>0.5284</b> (+0.0395)
	NIMA $\uparrow$	4.7026	4.3639	4.8282	4.8193	4.8957	4.4948	4.6401	5.0590	<b>5.1813</b>	5.1810 (+0.0003)
	CLIP-IQA $\uparrow$	0.5283	0.3521	0.6601	0.6806	<b>0.6993</b>	0.5390	0.4857	0.6631	0.6359	<b>0.6936</b> (+0.0577)
	NIQE $\downarrow$	9.0674	6.8733	6.4682	6.0700	5.4594	5.2873	5.2819	5.0912	4.8134	<b>3.9526</b> (-0.8608)
	UniPercept IQA $\uparrow$	46.5538	35.9550	52.3237	53.6550	58.0538	46.7850	56.6063	63.2025	60.0925	<b>64.7588</b> (+4.6663)
	VisualQuality-R1 $\uparrow$	3.4492	2.7112	3.5158	3.8928	4.0635	3.5028	3.7821	4.1953	4.1376	<b>4.3389</b> (+0.2013)
LucidConsistency $\uparrow$	0.8933	<b>0.9398</b>	0.8652	0.9013	0.8873	0.9261	0.8915	0.8902	0.9008	<b>0.9038</b> (+0.0030)	

our method achieves the best performance on most IQA metrics including CLIP-IQA+, Q-Align, MUSIQ, and UniPercept.

We also report **LucidConsistency** to measure LR-referenced semantic faithfulness. While LucidFlux(+LucidNFT) generally improves LucidConsistency over the LucidFlux baseline, StableSR occasionally attains higher scores. This is primarily explained by a *degradation-overlap confounder* inherent to LR-referenced similarity: if a method under-restores and preserves LR-like degradations (e.g., blur or compression artifacts), the output becomes more similar to the LR observation in representation space, which can inflate the LR-SR similarity score without necessarily improving restoration quality. We analyze this effect in Sec. 5.3. Importantly, LucidNFT optimizes LucidConsistency jointly with a perceptual quality reward (UniPercept IQA) under multi-reward learning, which discourages degenerate solutions that retain degradations to increase consistency.

**Degradation-Overlap Effect Analysis.** LucidConsistency is LR-referenced and compares the LR observation with the generated SR output in a learned semantic space. As a result, an inherent *degradation-overlap confounder* can arise under *under-restoration*: if the output preserves LR-like degradations (e.g., blur or compression artifacts), LR-SR representations may become more similar, increasing the LucidConsistency score without necessarily indicating better restoration quality. LucidNFT mitigates this confounder by optimizing LucidConsistency jointly with a perceptual quality reward (UniPercept) under multi-reward learning, discouraging degenerate solutions that retain degradations to inflate consistency. Meanwhile, Table 2 shows LucidConsistency remains

content-sensitive, assigning low similarity to cross-bench swapped pairs, suggesting the representation does not collapse to trivial matching. To further validate whether LucidConsistency captures LR-anchored faithfulness, we conduct a human preference study comparing model predictions with human judgments of LR-faithfulness. The study protocol and detailed results are reported in the supplementary material.

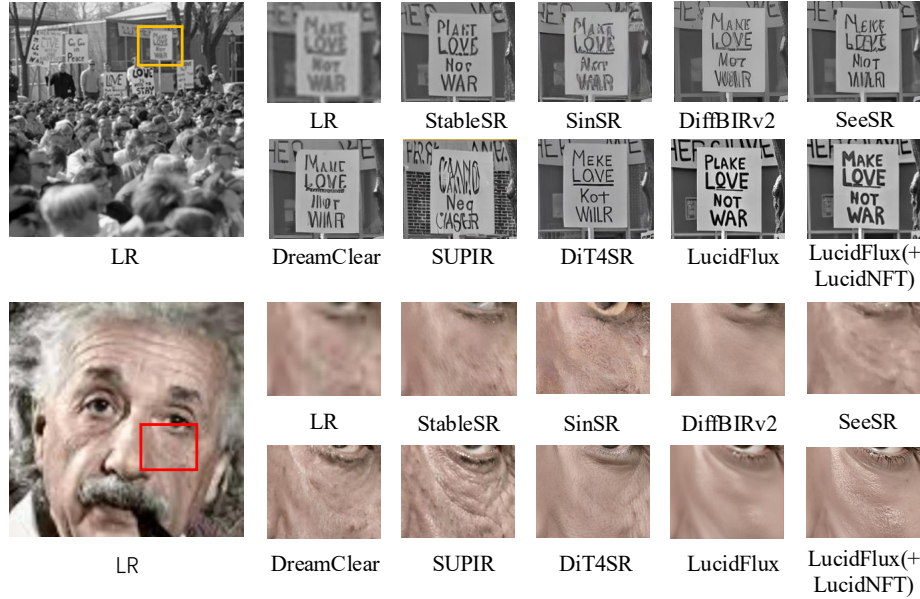


**Fig. 5:** Visual comparison on RealLQ250 [2]. LucidNFT further improves semantic consistency and perceptual quality over the baseline LucidFlux, producing more faithful structures and richer texture details.

**Qualitative Comparison.** Fig. 5 provides visual comparisons on RealLQ250 [2]. While the baseline LucidFlux already produces visually plausible restorations, LucidNFT further improves both perceptual quality and structural consistency. As shown in the first example, LucidNFT produces more faithful structures with reduced hallucinated artifacts. In the second example, our method reconstructs richer texture details while maintaining consistent global semantics with respect to the LR input. These results demonstrate that LucidNFT effectively balances perceptual enhancement and LR-conditioned faithfulness.

#### 5.4 Ablation Study

Table 4 analyzes key components in LucidNFT on RealLQ250 with LucidFlux as the backbone. All variants are trained under the same RL configuration for

**Table 4:** Ablation study of LucidNFT on RealLQ250 using LucidFlux as the backbone. All variants are trained under the same setting. Higher is better except NIQE.

Method	UniPercept $\uparrow$	VQ-R1 $\uparrow$	NIQE $\downarrow$	LucidConsistency $\uparrow$
LucidFlux (baseline)	70.930	4.547	3.741	0.9334
(A) IQA-only RL (UniPercept reward)	71.538	4.601	3.514	0.9259
(B) Multi-reward RL (scalar aggregation)	71.214	4.593	3.547	0.9341
(C) + Decoupled advantage normalization	72.703	4.633	3.372	0.9356
(D) + LucidLR (Full)	73.690	<b>4.671</b>	<b>3.241</b>	<b>0.9368</b>

fair comparison. The RL training is initialized from a LucidFlux model trained on synthesized LR from LSDIR [18] using the Real-ESRGAN [34] degradation pipeline. Optimizing with an IQA-only reward (A) improves perceptual quality compared with the baseline, but noticeably reduces LucidConsistency, indicating that improving perceptual sharpness alone can encourage LR-inconsistent details. Introducing a multi-reward objective with scalar aggregation (B) largely restores LR-referenced faithfulness, yet the overall perceptual gains become less pronounced. Replacing scalar-first aggregation with our decoupled multi-reward advantage normalization (C) significantly improves perceptual metrics while maintaining consistency, validating its ability to preserve objective-specific reward contrasts during optimization. Finally, training with the proposed LucidLR dataset (D) provides additional gains, particularly in NIQE and LucidConsistency, suggesting that diverse real-world degradations yield more informative rollouts and preference signals for RL-based alignment.

## 6 Conclusion

We present **LucidNFT**, a multi-reward reinforcement learning framework for aligning stochastic flow-based Real-ISR models. LucidNFT makes LR-anchored faithfulness *optimizable* via **LucidConsistency**, preserves perceptual-faithfulness trade-offs through **decoupled advantage normalization**, and enables robust fine-tuning under diverse real degradations with the **LucidLR** dataset. Experiments show consistent improvements over strong flow-based baselines on multiple real-world benchmarks, achieving better perceptual quality while maintaining LR-referenced consistency. We hope LucidNFT offers a practical route toward more reliable and controllable generative Real-ISR.

**Limitation.** LR-referenced faithfulness estimation remains challenging under severe or unseen degradations; improving degradation-robust consistency signals and richer preferences is an important direction for future work.

## References

1. Agustsson, E., Timofte, R.: Ntire 2017 challenge on single image super-resolution: Dataset and study. In: Proceedings of the IEEE Conference on Computer Vision and Pattern Recognition Workshops. pp. 126–135 (2017)

2. Ai, Y., Zhou, X., Huang, H., Han, X., Chen, Z., You, Q., Yang, H.: Dreamclear: High-capacity real-world image restoration with privacy-safe dataset curation. *Advances in Neural Information Processing Systems* **37**, 55443–55469 (2024)
3. Black, K., Janner, M., Du, Y., Kostrikov, I., Levine, S.: Training diffusion models with reinforcement learning. *arXiv preprint arXiv:2305.13301* (2023)
4. Cai, J., Zeng, H., Yong, H., Cao, Z., Zhang, L.: Toward real-world single image super-resolution: A new benchmark and a new model. In: *Proceedings of the IEEE/CVF International Conference on Computer Vision*. pp. 3086–3095 (2019)
5. Cao, S., Li, J., Li, X., Pu, Y., Zhu, K., Gao, Y., Luo, S., Xin, Y., Qin, Q., Zhou, Y., Chen, X., Zhang, W., Fu, B., Qiao, Y., Liu, Y.: Unipercept: Towards unified perceptual-level image understanding across aesthetics, quality, structure, and texture (2025)
6. Chen, J., Yu, J., Ge, C., Yao, L., Xie, E., Wu, Y., Wang, Z., Kwok, J., Luo, P., Lu, H., Li, Z.: Pixart- $\alpha$ : Fast training of diffusion transformer for photorealistic text-to-image synthesis (2023)
7. Chen, X., Wang, X., Zhou, J., Qiao, Y., Dong, C.: Activating more pixels in image super-resolution transformer. In: *Proceedings of the IEEE/CVF Conference on Computer Vision and Pattern Recognition*. pp. 22367–22377 (2023)
8. Cohen, R., Kligvasser, I., Rivlin, E., Freedman, D.: Looks too good to be true: An information-theoretic analysis of hallucinations in generative restoration models. *Advances in Neural Information Processing Systems* **37**, 22596–22623 (2024)
9. Dong, C., Loy, C.C., He, K., Tang, X.: Learning a deep convolutional network for image super-resolution. In: *Proceedings of the European Conference on Computer Vision*. pp. 184–199. Springer (2014)
10. Duan, Z.P., Zhang, J., Jin, X., Zhang, Z., Xiong, Z., Zou, D., Ren, J., Guo, C.L., Li, C.: Dit4sr: Taming diffusion transformer for real-world image super-resolution. In: *Proceedings of the IEEE/CVF International Conference on Computer Vision* (2025)
11. Esser, P., Kulal, S., Blattmann, A., Entezari, R., Müller, J., Saini, H., Levi, Y., Lorenz, D., Sauer, A., Boesel, F., et al.: Scaling rectified flow transformers for high-resolution image synthesis. In: *Forty-first International Conference on Machine Learning* (2024)
12. Falconsai: Nsfw image detection model (2026)
13. Fei, S., Ye, T., Wang, L., Zhu, L.: Lucidflux: Caption-free universal image restoration via a large-scale diffusion transformer. *arXiv preprint arXiv:2509.22414* (2025)
14. Hu, E.J., Shen, Y., Wallis, P., Allen-Zhu, Z., Li, Y., Wang, S., Wang, L., Chen, W., et al.: Lora: Low-rank adaptation of large language models. *Iclr* **1**(2), 3 (2022)
15. Ke, J., Wang, Q., Wang, Y., Milanfar, P., Yang, F.: Musiq: Multi-scale image quality transformer. In: *Proceedings of the IEEE/CVF International Conference on Computer Vision*. pp. 5148–5157 (2021)
16. Labs, B.F.: Flux (2024)
17. Li, M., Zhang, Y., Long, D., Chen, K., Song, S., Bai, S., Yang, Z., Xie, P., Yang, A., Liu, D., et al.: Qwen3-vl-embedding and qwen3-vl-reranker: A unified framework for state-of-the-art multimodal retrieval and ranking. *arXiv preprint arXiv:2601.04720* (2026)
18. Li, Y., Zhang, K., Liang, J., Cao, J., Liu, C., Gong, R., Zhang, Y., Tang, H., Liu, Y., Demandolx, D., Ranjan, R., Timofte, R., Van Gool, L.: Lsdire: A large scale dataset for image restoration. In: *Proceedings of the IEEE/CVF Conference on Computer Vision and Pattern Recognition*. pp. 1775–1787 (2023)

19. Lin, X., He, J., Chen, Z., Lyu, Z., Dai, B., Yu, F., Qiao, Y., Ouyang, W., Dong, C.: Diffbir: Toward blind image restoration with generative diffusion prior. In: European Conference on Computer Vision. pp. 430–448. Springer (2024)
20. Lipman, Y., Chen, R.T., Ben-Hamu, H., Nickel, M., Le, M.: Flow matching for generative modeling. arXiv preprint arXiv:2210.02747 (2022)
21. Liu, J., Liu, G., Liang, J., Li, Y., Liu, J., Wang, X., Wan, P., Zhang, D., Ouyang, W.: Flow-grpo: Training flow matching models via online rl. arXiv preprint arXiv:2505.05470 (2025)
22. Liu, X., Gong, C., Liu, Q.: Flow straight and fast: Learning to generate and transfer data with rectified flow. arXiv preprint arXiv:2209.03003 (2022)
23. Loshchilov, I., Hutter, F.: Decoupled weight decay regularization. arXiv preprint arXiv:1711.05101 (2017)
24. Oord, A.v.d., Li, Y., Vinyals, O.: Representation learning with contrastive predictive coding. arXiv preprint arXiv:1807.03748 (2018)
25. Podell, D., English, Z., Lacey, K., Blattmann, A., Dockhorn, T., Müller, J., Penna, J., Rombach, R.: Sdxl: Improving latent diffusion models for high-resolution image synthesis. arXiv preprint arXiv:2307.01952 (2023)
26. Rafailov, R., Sharma, A., Mitchell, E., Manning, C.D., Ermon, S., Finn, C.: Direct preference optimization: Your language model is secretly a reward model. *Advances in neural information processing systems* **36**, 53728–53741 (2023)
27. Rombach, R., Blattmann, A., Lorenz, D., Esser, P., Ommer, B.: High-resolution image synthesis with latent diffusion models. In: Proceedings of the IEEE/CVF Conference on Computer Vision and Pattern Recognition. pp. 10684–10695 (2022)
28. Schulman, J., Wolski, F., Dhariwal, P., Radford, A., Klimov, O.: Proximal policy optimization algorithms. arXiv preprint arXiv:1707.06347 (2017)
29. Sutton, R.S., Barto, A.G., et al.: Reinforcement learning: An introduction, vol. 1. MIT press Cambridge (1998)
30. Talebi, H., Milanfar, P.: Nima: Neural image assessment. *IEEE Transactions on Image Processing* **27**(8), 3998–4011 (2018)
31. Wallace, B., Dang, M., Rafailov, R., Zhou, L., Lou, A., Purushwalkam, S., Ermon, S., Xiong, C., Joty, S., Naik, N.: Diffusion model alignment using direct preference optimization. In: Proceedings of the IEEE/CVF Conference on Computer Vision and Pattern Recognition. pp. 8228–8238 (2024)
32. Wang, J., Chan, K.C., Loy, C.C.: Exploring clip for assessing the look and feel of images. In: AAAI (2023)
33. Wang, J., Yue, Z., Zhou, S., Chan, K.C., Loy, C.C.: Exploiting diffusion prior for real-world image super-resolution. *International Journal of Computer Vision* **132**(12), 5929–5949 (2024)
34. Wang, X., Xie, L., Dong, C., Shan, Y.: Real-esrgan: Training real-world blind super-resolution with pure synthetic data. In: Proceedings of the IEEE/CVF international conference on computer vision. pp. 1905–1914 (2021)
35. Wang, Y., Yang, W., Chen, X., Wang, Y., Guo, L., Chau, L.P., Liu, Z., Qiao, Y., Kot, A.C., Wen, B.: Sinsr: diffusion-based image super-resolution in a single step. In: Proceedings of the IEEE/CVF Conference on Computer Vision and Pattern Recognition. pp. 25796–25805 (2024)
36. Wang, Z., Bovik, A.C., Sheikh, H.R., Simoncelli, E.P.: Image quality assessment: from error visibility to structural similarity. *IEEE Transactions on Image Processing* **13**(4), 600–612 (2004)
37. Wei, P., Xie, Z., Lu, H., Zhan, Z., Ye, Q., Zuo, W., Lin, L.: Component divide-and-conquer for real-world image super-resolution. In: Proceedings of the European Conference on Computer Vision. pp. 101–117. Springer (2020)

38. Wu, H., Zhang, Z., Zhang, W., Chen, C., Li, C., Liao, L., Wang, A., Zhang, E., Sun, W., Yan, Q., Min, X., Zhai, G., Lin, W.: Q-align: Teaching lms for visual scoring via discrete text-defined levels. arXiv preprint arXiv:2312.17090 (2023), equal Contribution by Wu, Haoning and Zhang, Zicheng. Project Lead by Wu, Haoning. Corresponding Authors: Zhai, Guangtai and Lin, Weisi.
39. Wu, R., Yang, T., Sun, L., Zhang, Z., Li, S., Zhang, L.: Seesr: Towards semantics-aware real-world image super-resolution. In: Proceedings of the IEEE/CVF Conference on Computer Vision and Pattern Recognition. pp. 25456–25467 (2024)
40. Wu, T., Zou, J., Liang, J., Zhang, L., Ma, K.: VisualQuality-R1: Reasoning-induced image quality assessment via reinforcement learning to rank. arXiv preprint arXiv:2505.14460 (2025)
41. Xue, Z., Wu, J., Gao, Y., Kong, F., Zhu, L., Chen, M., Liu, Z., Liu, W., Guo, Q., Huang, W., et al.: Dancegrp0: Unleashing grp0 on visual generation. arXiv preprint arXiv:2505.07818 (2025)
42. Yang, S., Wu, T., Shi, S., Lao, S., Gong, Y., Cao, M., Wang, J., Yang, Y.: Maniqa: Multi-dimension attention network for no-reference image quality assessment. In: Proceedings of the IEEE/CVF Conference on Computer Vision and Pattern Recognition. pp. 1191–1200 (2022)
43. Yu, F., Gu, J., Li, Z., Hu, J., Kong, X., Wang, X., He, J., Qiao, Y., Dong, C.: Scaling up to excellence: Practicing model scaling for photo-realistic image restoration in the wild (2024)
44. Yue, Z., Wang, J., Loy, C.C.: Resshift: Efficient diffusion model for image super-resolution by residual shifting. *Advances in Neural Information Processing Systems* **36**, 13294–13307 (2023)
45. Zhang, K., Liang, J., Van Gool, L., Timofte, R.: Designing a practical degradation model for deep blind image super-resolution. In: Proceedings of the IEEE/CVF international conference on computer vision. pp. 4791–4800 (2021)
46. Zhang, L., Zhang, L., Bovik, A.C.: A feature-enriched completely blind image quality evaluator. *IEEE Transactions on Image Processing* **24**(8), 2579–2591 (2015)
47. Zhang, Y., Li, K., Li, K., Wang, L., Zhong, B., Fu, Y.: Image super-resolution using very deep residual channel attention networks. In: Proceedings of the European Conference on Computer Vision. pp. 286–301 (2018)
48. Zheng, K., Chen, H., Ye, H., Wang, H., Zhang, Q., Jiang, K., Su, H., Ermon, S., Zhu, J., Liu, M.Y.: Diffusionnft: Online diffusion reinforcement with forward process. arXiv preprint arXiv:2509.16117 (2025)

## A Supplemental Materials

### A.1 Human Preference Alignment on LR-Faithfulness

To examine whether *LucidConsistency* aligns with human judgments of LR-faithfulness, we conduct a human preference study on *RealLQ250*. The objective of this experiment is not to measure perceptual quality, but to evaluate whether a metric correctly identifies the SR result that is most faithful to the LR observation.

We randomly sample 30 LR images and collect the corresponding SR results from three representative methods: *ResShift*, *SeeSR*, and *LucidFlux(+LucidNFT)*. Three annotators with prior research experience in Real-SR are asked to rank the three SR candidates according to **consistency with the LR input only**. During annotation, they are instructed not to consider perceptual quality or sharpness, but instead to judge whether the SR result preserves structures and degradation characteristics that are plausible given the LR observation. The annotation interface is shown in Fig. 6.

We compare human rankings with two automatic criteria: (1) cosine similarity computed directly from the backbone embedding, and (2) *LucidConsistency*, which measures cosine similarity after the learned consistency projection head. Two agreement metrics are reported: **Top-1 agreement**, which measures whether the metric selects the same most faithful SR result as humans, and **pairwise agreement**, computed over the three pairwise comparisons induced by each ranking.

Results are summarized in Table 5. *LucidConsistency* shows better alignment with human judgments than the backbone baseline. The top-1 agreement improves from **11/30 (36.7%)** to **15/30 (50.0%)**. In terms of pairwise agreement, backbone cosine achieves **44/90 (48.9%)** while *LucidConsistency* achieves **55/90 (61.1%)**.

Evaluating LR-faithfulness is inherently challenging, as differences between SR results are often subtle and localized. During annotation, even experienced annotators frequently needed to inspect small regions to identify inconsistencies between the SR output and the LR input. This observation highlights a largely overlooked issue in Real-SR evaluation: existing metrics mainly measure perceptual quality or generic semantic similarity, while faithfulness to the LR observation remains underexplored. Our results suggest that explicitly modeling degradation-robust consistency provides a signal that better aligns with human LR-faithfulness judgments.

### A.2 Effectiveness of LucidNFT on DiT4SR

We further evaluate the generality of LucidNFT by applying the proposed RL framework to the DiT4SR backbone [10]. Compared with LucidFlux, which is built upon a large-scale generative backbone (14B parameters), DiT4SR adopts a more lightweight architecture derived from Stable Diffusion 3 Medium [11], consisting of a 2B prior and a 2.72B adapter. This experiment investigates whether

**Table 5:** Human preference alignment on LR-faithfulness over 30 samples from RealLQ250.

Metric	Top-1 agreement	Pairwise agreement
Backbone cosine	11/30 (36.7%)	44/90 (48.9%)
LucidConsistency	<b>15/30 (50.0%)</b>	<b>55/90 (61.1%)</b>

the proposed multi-reward RL formulation can consistently improve perceptual quality and LR-conditioned faithfulness across flow-based backbones of different capacities.

Training curves for DiT4SR are shown in Fig. 7. The optimization dynamics closely resemble those observed on LucidFlux: the image quality reward (UniPercept IQA) steadily increases during training, while the consistency reward remains relatively stable with moderate stochastic fluctuations caused by generative sampling.

We note that the validation LucidConsistency score exhibits a slight decrease during training. This behavior is expected due to the lightweight evaluation configuration used during training. Specifically, validation rewards are computed with a reduced setting of *768 resolution* and *15 inference steps*, while the final testing configuration uses *1024 resolution* and *40 inference steps*. Such a simplified evaluation protocol introduces additional variance and may underestimate the consistency score during training. Importantly, the final quantitative results reported in Table 6 still show consistent improvements in LucidConsistency after applying LucidNFT, confirming that the learned policy improves restoration faithfulness under the full inference setting.

Table 6 reports quantitative results before and after applying LucidNFT on three Real-SR benchmarks: RealLQ250 [2], DRealSR [37], and RealSR [4]. Consistent improvements are observed across multiple perceptual quality metrics after RL optimization.

On RealLQ250, the UniPercept IQA score increases from 73.07 to **73.34**, while NIQE decreases from 3.56 to **3.50**, indicating improved perceptual realism and more natural image statistics. Similar improvements are observed on RealSR and DRealSR. For example, on RealSR the UniPercept IQA score increases from 63.20 to **64.84**, accompanied by gains in CLIP-IQA and MUSIQ while maintaining competitive NIQE values. These results demonstrate that the proposed multi-reward RL optimization generalizes well across flow-based Real-ISR backbones and consistently improves restoration quality without sacrificing naturalness.

### A.3 Degradation Statistics of LucidLR and Comparison with Existing Real-ISR Datasets

We analyze the degradation diversity of LucidLR by annotating four representative real-world low-quality datasets, including LucidLR, RealLQ250, RealSR,

**Table 6:** Quantitative comparison with state-of-the-art Real-ISR methods on RealLQ250 [2], DRealSR [37], and RealSR [4]. Higher is better for all metrics except NIQE. Values in parentheses indicate improvements over the corresponding backbone baseline. Best and second-best results are highlighted in bold and underline, respectively. Values in parentheses denote improvements over the corresponding backbone baseline.

Benchmark	Metric	ResShift	StableSR	SinSR	DHBRv2	SeeSR	DreamClear	SUPIR	DiT4SR	DiT4SR(+LucidNFT)	LucidFlux	LucidFlux(+LucidNFT)
RealLQ250	CLIP-IQA+ $\uparrow$	0.5529	0.5804	0.6054	0.6019	0.7034	0.6813	0.6532	0.7098	0.7124 (+0.0026)	<u>0.7208</u>	<b>0.7465</b> (+0.0257)
	Q-Align $\uparrow$	3.6318	3.5583	3.7451	3.9755	4.1423	4.0647	4.1347	4.2270	4.2358 (+0.0088)	<u>4.4052</u>	<b>4.4855</b> (+0.0803)
	MUSIQ $\uparrow$	59.5032	57.2517	65.4543	67.5313	70.3757	67.0809	65.8133	71.6682	72.1732 (+0.5050)	<u>72.3351</u>	<b>73.4475</b> (+1.1124)
	MANIQA $\uparrow$	0.3397	0.2937	0.4230	0.4900	0.4895	0.4405	0.3826	0.4607	0.4719 (+0.0112)	<u>0.5227</u>	<b>0.5443</b> (+0.0216)
	NIMA $\uparrow$	5.0624	5.0538	5.2397	5.3132	5.3146	5.2209	5.0806	5.4765	5.4504 (+0.0261)	<u>5.6050</u>	<b>5.5669</b> (+0.0381)
	CLIP-IQA $\uparrow$	0.6129	0.5160	<u>0.7166</u>	0.7137	0.7063	0.6957	0.5767	0.7141	<b>0.7355</b> (+0.0214)	0.6855	0.7233 (+0.0378)
	NIQE $\downarrow$	6.6326	4.8296	5.4425	5.1193	4.4383	3.8769	3.6591	<u>3.5556</u>	3.5047 (+0.0509)	3.7410	<b>3.7332</b> (+0.0478)
	UniPercept IQA $\uparrow$	58.9290	57.6015	62.7525	65.4760	69.2015	68.8465	68.6430	<u>73.0740</u>	73.3430 (+0.2690)	70.9300	<b>73.4790</b> (+2.5490)
	VisualQuality-R1 $\uparrow$	4.0911	3.9474	3.9044	4.3428	4.5118	4.4430	4.4265	<u>4.6146</u>	4.6304 (+0.0158)	4.5474	<b>4.6510</b> (+0.1036)
	LucidConsistency $\uparrow$	0.9340	<b>0.9496</b>	0.9232	<u>0.9430</u>	0.9352	0.9467	0.9376	0.9359	0.9362 (+0.0003)	0.9334	0.9366 (+0.0032)
DRealSR	CLIP-IQA+ $\uparrow$	0.4655	0.3732	0.5402	0.6476	0.6258	0.4462	0.5494	0.6537	0.6757 (+0.0220)	<u>0.6516</u>	<b>0.6867</b> (+0.0351)
	Q-Align $\uparrow$	2.6312	2.1243	3.1336	3.0487	3.2746	2.4214	3.4722	3.6008	3.6641 (+0.0633)	<u>3.7441</u>	<b>3.8423</b> (+0.1282)
	MUSIQ $\uparrow$	40.9795	29.6691	53.9139	60.0759	61.3222	35.1912	54.9280	63.8051	65.1915 (+1.3864)	<u>64.6025</u>	<b>68.1545</b> (+3.5520)
	MANIQA $\uparrow$	0.2688	0.2402	0.3456	<u>0.4301</u>	0.4505	0.2676	0.3483	0.4419	0.4572 (+0.0153)	0.4678	<b>0.5004</b> (+0.0326)
	NIMA $\uparrow$	4.3179	3.9049	4.9227	4.6543	4.6402	3.9369	4.5064	<u>4.9013</u>	4.9870 (+0.0806)	4.9560	<b>4.9968</b> (+0.0408)
	CLIP-IQA $\uparrow$	0.4964	0.3383	0.6632	0.6782	0.6760	0.4361	0.5310	0.6732	<b>0.7111</b> (+0.0379)	0.6673	<u>0.7073</u> (+0.0400)
	NIQE $\downarrow$	10.3006	8.6023	6.9800	6.4853	6.4503	7.0164	5.9092	<u>5.7001</u>	5.6329 (+0.0672)	5.0742	<b>4.1788</b> (+0.8954)
	UniPercept IQA $\uparrow$	37.3199	26.0659	49.2755	46.2298	50.3414	34.2473	55.1371	58.1290	59.9328 (+1.8038)	<u>59.9032</u>	<b>63.7782</b> (+3.8750)
	VisualQuality-R1 $\uparrow$	3.0231	1.8758	3.3868	3.4796	3.6116	2.5655	3.7349	3.9603	4.0239 (+0.0636)	<u>3.9555</u>	<b>4.1455</b> (+0.1900)
	LucidConsistency $\uparrow$	0.8897	<b>0.9413</b>	0.8604	<u>0.9403</u>	0.8926	0.9403	0.8909	0.8886	0.8909 (+0.0023)	0.7998	0.7916 (+0.0082)
RealSR	CLIP-IQA+ $\uparrow$	0.5005	0.4408	0.5416	0.6543	0.6731	0.5331	0.5640	0.6753	0.6881 (+0.0128)	<u>0.6660</u>	<b>0.7151</b> (+0.0482)
	Q-Align $\uparrow$	3.1041	2.5086	3.3614	3.3156	3.6073	3.0040	3.4682	3.7106	3.7959 (+0.0853)	<u>3.8728</u>	<b>3.9918</b> (+0.1190)
	MUSIQ $\uparrow$	49.4888	39.9816	57.9502	61.7751	67.5660	49.4766	55.8807	67.9828	69.1092 (+1.1264)	<u>67.2862</u>	<b>70.5625</b> (+3.2663)
	MANIQA $\uparrow$	0.2976	0.2356	0.3753	0.4745	<u>0.5087</u>	0.3092	0.3426	0.4533	0.4654 (+0.0121)	0.4889	<b>0.5284</b> (+0.0395)
	NIMA $\uparrow$	4.7026	4.3639	4.8282	4.8193	4.8957	4.4948	4.6401	5.0590	5.0525 (+0.0065)	<b>5.1813</b>	<u>5.1810</u> (+0.0003)
	CLIP-IQA $\uparrow$	0.5283	0.3521	0.6601	0.6806	<b>0.6993</b>	0.5390	0.4857	0.6631	0.6963 (+0.0332)	0.6359	<u>0.6936</u> (+0.0577)
	NIQE $\downarrow$	9.0674	6.8733	6.4682	6.0700	5.2873	5.2819	5.0912	4.8332 (+0.2580)	<u>4.8134</u>	<b>3.9526</b> (+0.8608)	
	UniPercept IQA $\uparrow$	46.5538	35.9550	52.3237	53.6550	58.0538	46.7850	56.6063	63.2025	<b>64.8425</b> (+1.6400)	60.0925	<u>64.2585</u> (+4.1663)
	VisualQuality-R1 $\uparrow$	3.4492	2.7112	3.5158	3.8928	4.0635	3.5028	3.7821	4.1953	4.3429 (+0.0476)	<u>4.1372</u>	<b>4.3389</b> (+0.2013)
	LucidConsistency $\uparrow$	0.8933	<b>0.9398</b>	0.8652	<u>0.9261</u>	0.8873	0.9261	0.8915	0.8902	0.8938 (+0.0036)	0.9008	0.9038 (+0.0030)

and DRealSR, using a unified degradation taxonomy. The resulting category distributions are compared in Fig. 9 and Fig. 8.

**Annotation protocol.** We employ `gemini-2.5-flash` as a visual degradation classifier to annotate each image. For every sample, the model predicts (1) a single **primary degradation** and (2) a set of **degradation types** under a multi-label setting. The predictions are aggregated into two complementary statistics: **occurrence frequency**, which records whether a degradation appears in an image at least once, and **primary degradation distribution**, which counts only the dominant degradation assigned to each image.

**Prompt used for annotation.** We use the following prompt directly without manual modification:

### Prompt A.1 (Identifying Real-World Image Degradations)

You are an expert in low-level vision and image restoration. Carefully analyze the input image and identify visible degradation types present in the image. Your task is to determine both the **dominant degradation** and the **set of visible degradations**. Only consider degradations that are clearly observable from visual evidence.

Use only the following degradation labels exactly:

– `motion_blur`, `defocus_blur`

- noise
- jpeg\_artifacts, compression\_artifacts
- aliasing
- haze, fog
- rain\_streaks, snow
- low\_light, overexposure
- color\_cast, color\_distortion
- dirty\_lens, occlusion, lens\_flare
- other, none

Label guidance:

- **motion\_blur**: directional blur caused by camera or object motion
- **defocus\_blur**: out-of-focus blur or shallow depth-of-field
- **noise**: visible sensor noise, grain, chroma noise
- **jpeg\_artifacts**: JPEG blocking, mosquito noise, DCT artifacts
- **compression\_artifacts**: generic codec artifacts beyond JPEG
- **aliasing**: jagged edges or resampling artifacts
- **haze / fog**: atmospheric scattering reducing contrast
- **rain\_streaks / snow**: visible precipitation structures
- **low\_light**: severe underexposure or dark scenes
- **overexposure**: clipped highlights or blown-out regions
- **color\_cast**: global color tint due to white balance failure
- **color\_distortion**: abnormal color reproduction
- **dirty\_lens**: stains, droplets, or smears on the lens
- **occlusion**: partial obstruction by objects
- **lens\_flare**: bright streaks or glare caused by strong light
- **other**: degradation exists but does not match the above labels
- **none**: image is mostly clean with no obvious degradation

Return results strictly in the following JSON format, without any additional explanation or text:

```
{
  "primary_degradation": "one label from the list",
  "degradation_types": ["label1", "label2"],
  "confidence": 0.0,
  "reason": "brief evidence-based explanation"
}
```

Annotation rules:

- Always return exactly 1 **primary\_degradation**.
- Return 1-6 **degradation\_types** when degradation exists.
- Multiple degradations may appear simultaneously; include all clearly visible degradations.
- **primary\_degradation** must correspond to the dominant degradation among the listed types.
- Order **degradation\_types** from strongest to weakest visual impact.
- If the image is mostly clean, set:
  - **primary\_degradation** = "none"
  - **degradation\_types** = ["none"]

- Do not invent labels outside the predefined list.
  - Be conservative and rely only on visible evidence.
- Important:** Only return pure JSON format results, without markdown code blocks or additional commentary.

**Primary degradation distribution.** Figure 8 shows the primary degradation distribution, where each image contributes to exactly one dominant category. This view further highlights the difference in diversity between LucidLR and prior datasets. In LucidLR, the dominant degradations are distributed across multiple categories, including `defocus_blur` (31.5%), `jpeg_artifacts` (15.8%), `noise` (12.6%), `motion_blur` (9.0%), `low_light` (8.7%), and `compression_artifacts` (5.6%). By comparison, RealSR and DRealSR are overwhelmingly dominated by `defocus_blur` as the primary degradation (84.0% and 76.3%, respectively), indicating much narrower degradation modes. RealLQ250 covers more categories, but remains substantially smaller than LucidLR.

**Occurrence frequency.** Figure 9 reports the occurrence frequency of each degradation type, i.e., the percentage of images in which a degradation appears at least once. Since this is a multi-label statistic, the percentages do not sum to 100%. Compared with existing benchmark datasets, LucidLR exhibits substantially broader and more realistic degradation coverage. In LucidLR, high-frequency degradations include `noise` (75.6%), `defocus_blur` (63.0%), `jpeg_artifacts` (34.4%), `low_light` (34.1%), and `compression_artifacts` (32.6%), while many other categories such as `aliasing`, `color_cast`, and `color_distortion` also appear with non-trivial frequency. In contrast, RealSR and DRealSR are much more concentrated, with `defocus_blur` dominating their occurrence statistics (92.0% and 82.8%, respectively). RealLQ250 is more diverse than RealSR and DRealSR, but its small scale still limits long-tail coverage.

**Discussion.** These results support the role of LucidLR as a large-scale real-world training source for Real-ISR. Beyond its substantially larger size, LucidLR contains richer and more mixed degradation patterns than existing benchmark-oriented datasets. Such diversity is particularly valuable for RL-based or unsupervised fine-tuning, where informative rollout variation and broad reward contrast depend on the presence of heterogeneous real-world degradations.

#### A.4 Additional Qualitative Results

We provide additional qualitative comparisons on the RealLQ250 dataset to further illustrate the behavior of LucidNFT. Fig. 10 presents representative examples comparing the LucidFlux baseline and the model optimized with LucidNFT. Compared with the baseline, LucidFlux(+LucidNFT) produces SR images with more faithful structures and clearer local details while maintaining strong perceptual quality. In particular, the RL-optimized model better preserves structural

patterns that are consistent with the LR observation, while reducing implausible hallucinated textures that occasionally appear in generative restoration models. These additional examples further support the quantitative results reported in the main paper, demonstrating that LucidNFT improves restoration fidelity without sacrificing perceptual realism.

### A.5 Optimization Curves under Different Reward Formulations

We analyze the optimization behavior of different reward formulations by examining the evolution of UniPercept rewards during RL training on the LucidFlux backbone. Three RL variants are compared: (A) IQA-only RL using the UniPercept reward, (B) multi-reward RL with scalar aggregation of UniPercept and LucidConsistency, and (C) the proposed LucidNFT with decoupled multi-reward advantage normalization. All variants are trained under the same RL configuration described in the main paper.

**Optimization Behavior.** Figure 11 shows the UniPercept reward trajectories during training and evaluation. Optimizing with an IQA-only reward (A) improves the UniPercept score compared with the pretrained baseline, indicating that RL effectively enhances perceptual quality. Introducing LucidConsistency through scalar reward aggregation (B) slightly reduces the UniPercept reward, reflecting the expected trade-off between perceptual sharpness and LR-referenced faithfulness. With the proposed decoupled advantage normalization (C), the UniPercept reward increases again and surpasses both variants, suggesting that preserving objective-wise reward contrasts enables more effective multi-reward optimization.

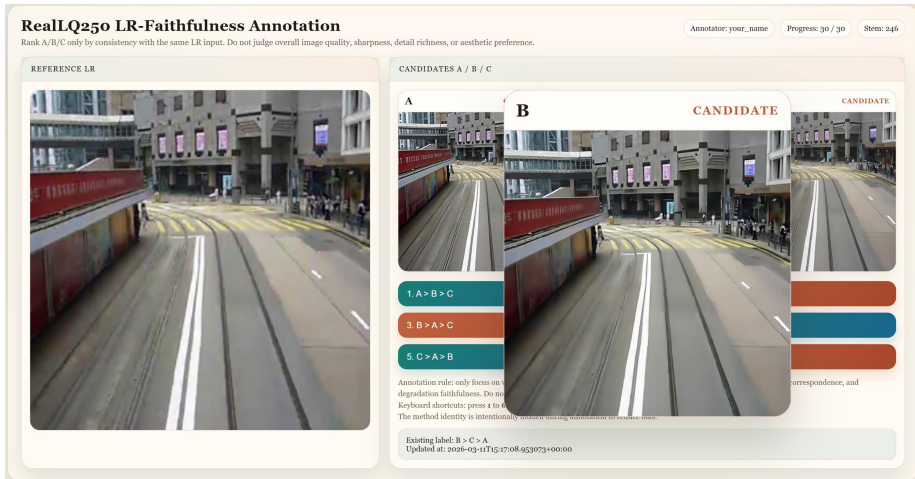
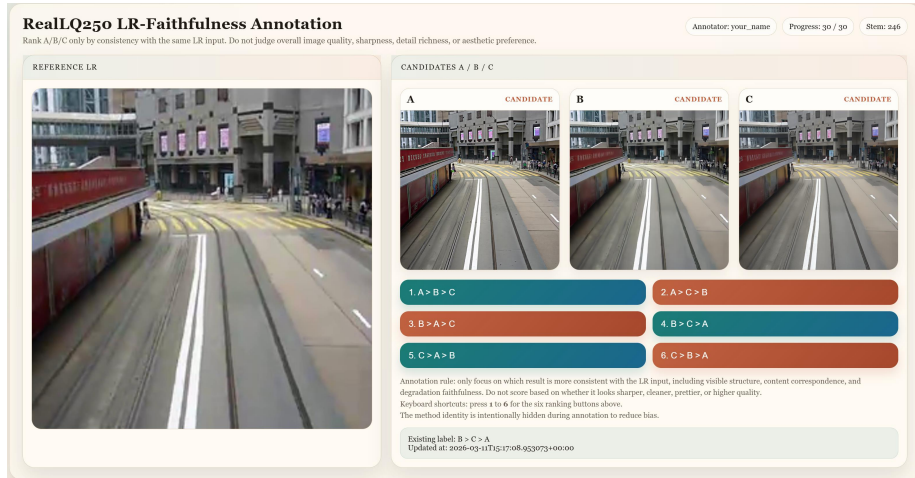


**Fig. 6:** Annotation interface used for the LR-faithfulness study. The first page shows the standard interface displaying the LR input and three SR candidates. The second page illustrates the enlarged view used by annotators to inspect local structures.



**Fig. 7:** Training dynamics of LucidNFT on the DiT4SR backbone. The curves show the evolution of the image quality reward (UniPercept IQA) and the consistency reward (LucidConsistency) during RL optimization.

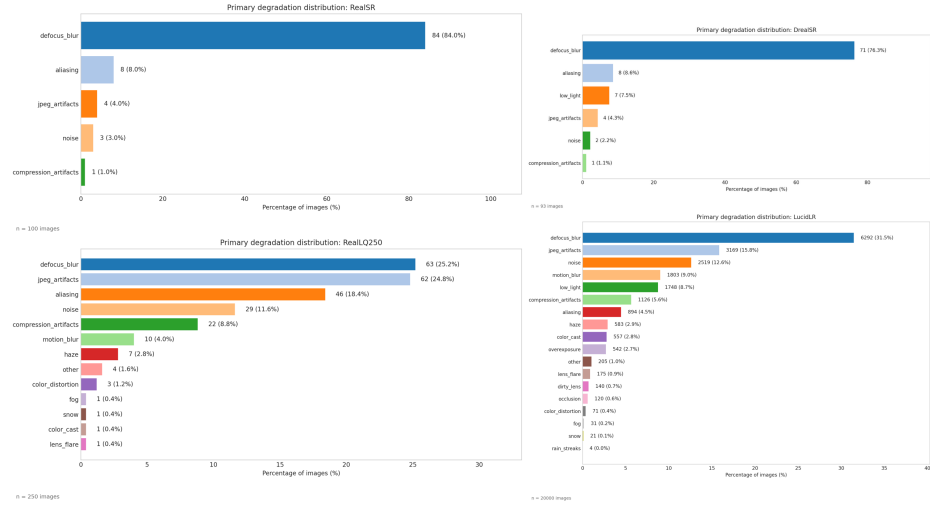


**Fig. 8:** Primary degradation distribution across four real-world low-quality datasets. Each image contributes to exactly one dominant degradation category. Compared with RealSR and DRealSR, which are strongly dominated by defocus blur, LucidLR presents a more balanced primary degradation distribution over multiple categories.

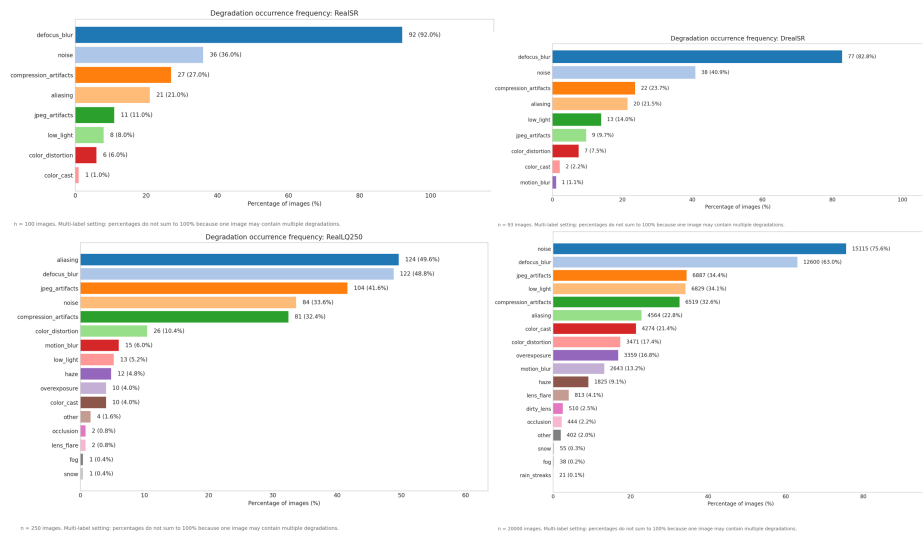


**Fig. 9:** Occurrence frequency of degradation categories across four real-world low-quality datasets: LucidLR, RealLQ250, RealSR, and DRealSR. Occurrence frequency is computed in a multi-label manner, so percentages do not sum to 100%. LucidLR exhibits substantially broader degradation coverage and a richer long-tail distribution than existing benchmark datasets.

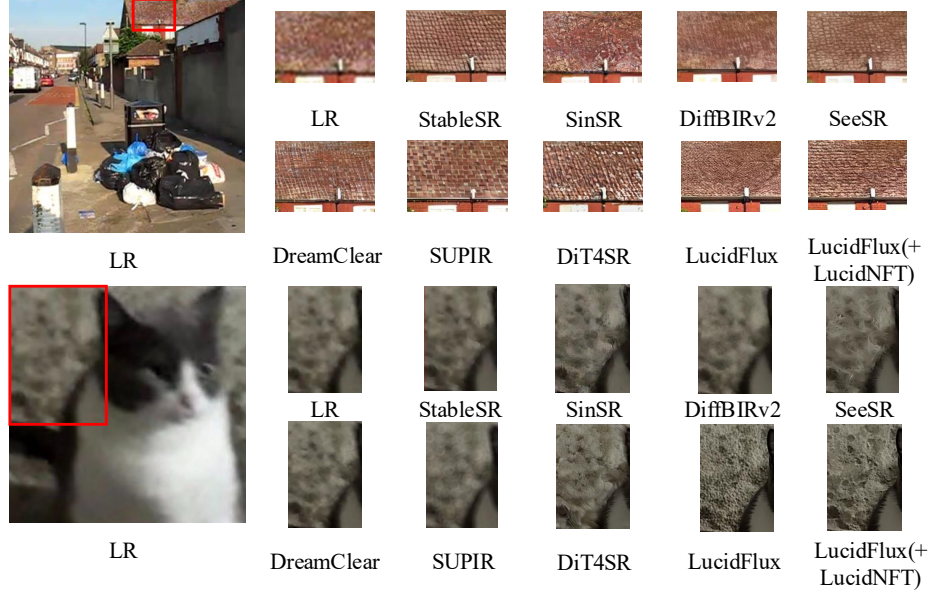


**Fig. 10:** Additional qualitative comparisons on RealLQ250 [2]. Compared with the LucidFlux baseline, LucidNFT consistently produces more faithful structures and richer texture details while maintaining strong perceptual quality. See Fig. 5 in the main paper for the primary qualitative results.

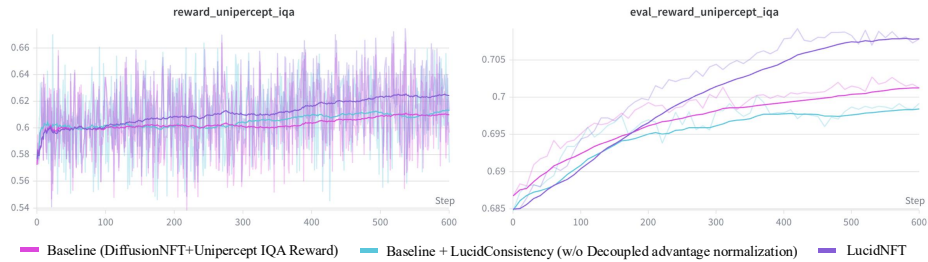


**Fig. 11:** Optimization curves under different reward formulations. The plots show UniPercept rewards during RL training (left) and evaluation (right). LucidNFT achieves higher rewards and smoother convergence compared with IQA-only RL and scalar-aggregated multi-reward RL.